CrossMark

RESEARCH PAPER

Synthesis and properties of $Sn_{1-x}Fe_xO_2$ nanoparticles obtained by a proteic sol–gel method

M. S. Pereira [ID] · **T. S. Ribeiro · F. A. S. Lima ·**
L. P. M. Santos · C. B. Silva · P. T. C. Freire ·
I. F. Vasconcelos

Abstract Iron-doped SnO$_2$ nanoparticles with chemical formula $Sn_{1-x}Fe_xO_{2-y}$ (x = 0.02, 0.05 and 0.10 at%) were successfully produced by a proteic sol–gel method. Thermogravimetric analysis and differential scanning calorimetry were performed to investigate the thermal behavior of the precursor powders as well as to select the appropriate calcination temperatures for oxide formation. X-ray absorption near-edge spectroscopy studies were carried out to determine the valence state of the transition metal used as dopant. Structural, morphological, and optical properties of the synthesized materials were studied by X-ray diffraction, Mössbauer spectroscopy, transmission electron microscopy, Fourier-transform infrared spectroscopy, and ultraviolet-visible spectroscopy. The results confirmed the formation of nanometric spherical particles of single-phased SnO$_2$ with rutile-type tetragonal structure. Iron doping was accomplished in the form of Fe^{3+} substituting for Sn^{4+} in the SnO$_2$ matrix, with the creation of oxygen vacancies to achieve charge balance. Band gaps of SnO$_2$ were found to be unaffected by the introduction of iron.

M. S. Pereira (✉) · C. B. Silva · P. T. C. Freire
Department of Physics, Universidade Federal do Ceará,
Fortaleza, Brazil
e-mail: mauriciosousa@alu.ufc.br

M. S. Pereira · I. F. Vasconcelos · T. S. Ribeiro
Department of Metallurgical and Materials Engineering,
Universidade Federal do Ceará, Fortaleza, Brazil

F. A. S. Lima
Dortech Technology, Salvador, Bahia, Brazil

L. P. M. Santos
Department of Chemistry, Universidade Federal do Ceará,
Fortaleza, Brazil

Introduction

Oxide-diluted magnetic semiconductors (O-DMS), where transition metal (TM) atoms of 3d valence electrons are introduced into the cationic sites of the semiconducting host lattice, have attracted the interest of researchers due to their potential use in future spintronic and magneto-optical devices (Ohno 2010; Oganisian et al. 2015). In general, O-DMS combine good electrical conductivity (Othmen et al. 2016), ferromagnetism (Mehraj et al. 2013, 2015), and high optical transparency (Feng et al. 2015), thereby opening up many different applications in contemporary and emerging technologies. Among the different oxide semiconductor materials, the oxides with wide band gap such as SnO$_2$ have been the subject of recent investigation due to their potential applications in the emerging fields (Pereira et al. 2017a; Tran et al. 2018).

Tin dioxide (SnO_2), normally known as cassiterite, is a typical n-type semiconductor with a direct wide band gap of 3.6 eV at room temperature (RT) and is one of the most widely used semiconductor oxide due to its chemical and mechanical stability (Chang et al. 2015; Aragon et al. 2016). Cassiterite has a rutile-type tetragonal crystal structure with a D_{4h}^{14} point group and $P4_2/mnm$ space group (Beltrán et al. 2010). Tin oxide has many technological applications, such as photovoltaic solar cells (Pereira et al. 2017a, b; Tran et al. 2018), gas sensors of toxic materials (Sun et al. 2014), liquid crystal displays, and anodes for lithium ion batteries (Mueller et al. 2015).

The synthesis of pure and doped SnO_2 has been carried out by different methods such as solid-state reaction methods (Ahmed 2010), chemical precipitation (Ferrari et al. 2016; Shayesteh and NosratiThe 2015), conventional sol–gel (Inpasalin et al. 2016; Mehraj et al. 2015), and mechanical milling (Ribeiro et al. 2012; Pereira et al. 2017a). It is well known that the synthesis method and the precursors employed in the preparation of these semiconductors can determine the physico-chemical, morphological, and electrical properties of the final product.

The solid-state reaction method involves milling and sintering for the production of compounds. Generally, high sintering temperatures are required which can lead to the growth of the particles to dimensions larger than the nanometric scale.

Chemical precipitation is a technique used in the production of several materials from the removal of dissolved (ionic) metals from solutions. The effectiveness of a chemical precipitation process is dependent on several factors, including the type and concentration of ionic metals present in solution, and the precipitant used, as well as the reaction conditions (especially the pH of the solution).

Mechanical milling is a technique for the production of powdered materials. In a typical mechanical milling experiment, reactant powders and milling balls are inserted in a jar and submitted to grinding in a ball mill. Furthermore, the materials produced by this method may result in particles with non-homogeneous dimensions.

Sol–gel methods have several advantages over other methods such as potential to produce compounds of high purity and with homogeneity at the atomic scale as well as significant reduction of processing times and temperatures required. There are variations in synthesis route, for example, the conventional sol–gel method employs alkoxides as precursor while proteic sol–gel employs an organic material as precursor.

The proteic sol–gel method (Meneses et al. 2007) is a variation of the conventional method which employs edible gelatin or coconut water as organic precursor for oxide formation. This low-cost method has been successfully employed in the synthesis of semiconductor materials with nanometric size, and showing potential for use in various technological applications (Pereira et al. 2017b). It involves a relatively simple method and has been successfully used to obtain homogeneous nanoparticles using more affordable reagents like nitrates and chlorides. The synthesis process consists of four stages: dissolution of the precursor salts in distilled water; formation of metal chelates by addition of gelatin; drying the material to remove water; and calcination to form the desired oxide. Calcination temperatures are usually only high enough to evaporate the organic matter.

This research work presents the synthesis and characterization of undoped and Fe–doped SnO_2 nanoparticles produced by the proteic sol–gel method. The doping of Fe in SnO_2 brought significant changes in the physical and chemical properties of the samples. Therefore, a systematic investigation of structural, morphological, and optical properties of these oxides has been undertaken, and the results are presented here.

Experimental procedure

Samples of $Sn_{1-x}Fe_xO_{2-y}$ (where y is the concentration of oxygen vacancies which depend on synthesis conditions) were prepared by the proteic sol–gel method (Meneses et al. 2007). A simplified illustration of the method is shown in Fig. 1. Commercial $SnCl_4 \cdot 5H_2O$ and $FeCl_3$ (Sigma-Aldrich, 99%) were employed as source of Sn^{4+} and Fe^{3+} ions, and commercial gelatin from $Gelita^{TM}$ as organic precursor. All reagents were used without any prior or further treatments. The gelatin was dispersed in distilled water under continuous stirring at room temperature until a uniform gel was obtained. The chlorides were dissolved separately in distilled water to make Sn^{4+} and Fe^{3+} solutions. Each solution containing metal ions was added to the gel in appropriate amounts to

Fig. 1 Schematic representation of the steps involved in the proteic sol–gel method
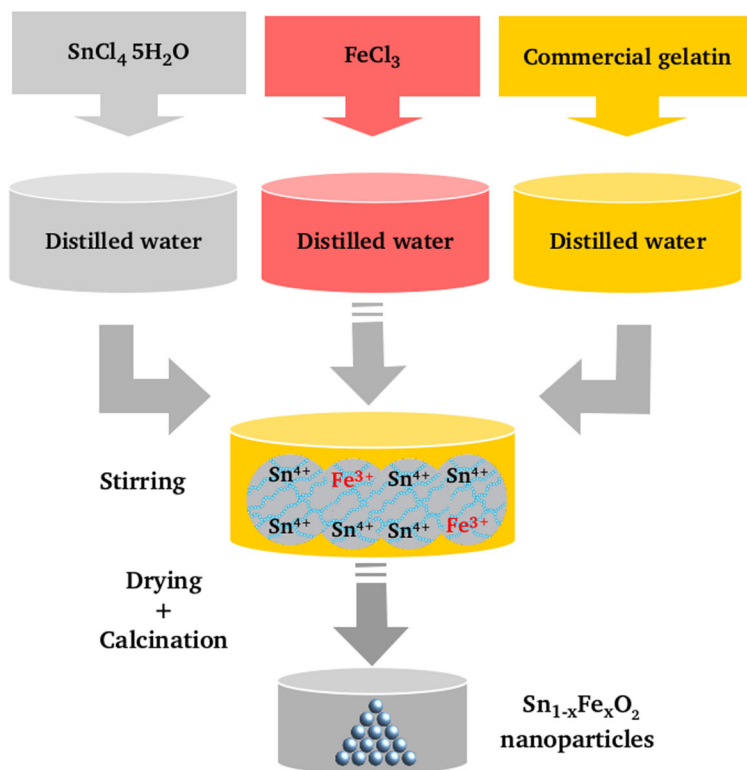
achieve the desired stoichiometries and maintained under continuous stirring at room temperature for 10 h to promote polyesterification.

The compound formed by the mixture of the chlorides and gelatin was then dried at 150 °C in air during 12 h to remove excess water and volatile components, resulting in a black solid puffy mass, referred to in this text as the precursor powder. The precursor powders were calcined at 350 °C in air atmosphere for 4 h, resulting in the $Sn_{1-x}Fe_xO_{2-y}$ nanoparticles. At these temperatures, the gelatin is not fully evaporated, therefore the samples were immersed in H_2O_2 to remove the residual organic matter. Finally, the samples were washed with distilled water and dried at a temperature of 150 °C in air atmosphere for 12 h.

Thermogravimetric analysis (TGA) and differential scanning calorimetry (DSC) were performed in the precursor powders in order to determine the temperature of oxide formation. Measurements were carried out using a NETZSCH STA 449F3 Jupiter thermal analysis equipment. Measurements were performed under air with heating hate of 5 °C/min. Valences of doping metals were determined by X-ray absorption near-edge spectroscopy (XANES). Room temperature XANES data on the Fe K-edge (7112 eV) were

collected at the XAFS2 beamline of the Brazilian Synchrontron Light Source (LNLS) in fluorescence mode.

X-ray diffraction (XRD) patterns were collected at room temperature using a Rigaku DMAXB diffractometer operating with a Kα-Cu source (λ = 1.54 Å) at 40 kV and 30 mA. The patterns were Rietveld refined (Rietveld 1967, 1969) using the program GSAS (Toby 2001). Rietveld refinement procedures were based on the SnO_2 standard crystal structures cataloged by the Inorganical Crystal Structure Database under number 39173 (ICSD-39173). Particle sizes were estimated by Scherrer's relation and, whenever possible, corrected by the Williamson-Hall method (Williamson and Hall 1953) which separates contributions of particle size and residual microstrain to the breadth of diffraction peaks.

Transmission electron microscopy (TEM) was performed using a 200-kV JEM 2011 microscope. Fourier-transform infrared (FT–IR) absorption spectra were collected at room temperature in transmission mode using a Bruker Vertex 70 spectrometer. Ultraviolet-visible (UV–vis) spectroscopy was carried out at room temperature in the diffuse reflectance mode using a UV 2600 Shimadzu spectrophotometer coupled to an

integrating sphere ISR 2600 Plus. Room temperature Mössbauer spectra were measured in transmission mode using a ^{57}Co(Rh) radioactive source mounted on a velocity driver operating in sinusoidal mode. The data were evaluated by least square fitting to a series of discrete Lorentzian-shaped subspectra by means of the software package Normos. Isomer shifts (δ) are quoted with respect to α-Fe.

Results and discussion

Thermal analysis

Figure 2 shows TGA/DSC curves of (a) undoped and (b) Fe–doped SnO_2 (5 at% of Fe) precursor powders. The thermal behavior of both samples may be divided into three main stages as indicated in Fig. 2: thermal degradation of gelatin chains (endothermic reaction); oxide formation (exothermic reaction); and carbonate decomposition with release of carbonyl groups (exothermic reaction).

In fact, DSC curves present endothermic peaks at about 250 °C (undoped sample) and 260 °C (doped sample) due to gelatin decomposition, exothermic peaks at about 370 °C (undoped) and 400 °C (doped) due to the formation and crystallization of SnO_2 (Zhao et al. 2015; Liu et al. 2016); and exothermic peaks around 580 °C (undoped) and 520 °C (doped) due to carbonate decomposition releasing carbonyl groups (Liu et al. 2015; Pereira et al. 2017b; Zhao et al. 2015).

While the peak at 400°C in the doped sample DSC can be associated with the formation of Fe-doped SnO_2, some Fe_2O_3 may also be formed in this stage (Song et al. 2012). Finally, the shift in temperature of the peak around 520 °C suggests that carbonyl decomposition is accelerated due to the presence of Fe^{3+} ions.

These results suggest a calcination temperature range of 300–400 °C. Preliminary tests showed the presence of a large amount of residual organic matter in samples calcined at 300 °C and of Fe_2O_3 in samples calcined 400 °C. Samples calcined at 350 °C showed just a small amount of organic matter and were clean of Fe_2O_3. Therefore, a calcination temperature of 350 °C was chosen.

XANES

Figure 3 shows Fe K-edge XANES spectra of a Fe-doped SnO_2 (5 at% of Fe) sample together with spectra of selected iron oxide standards. It is clear that the sample's energy absorption edge coincides with that of a Fe^{3+} reference standard. All other samples presented similar XANES spectra to the one shown confirming that iron enters the SnO_2 host as Fe^{3+}.
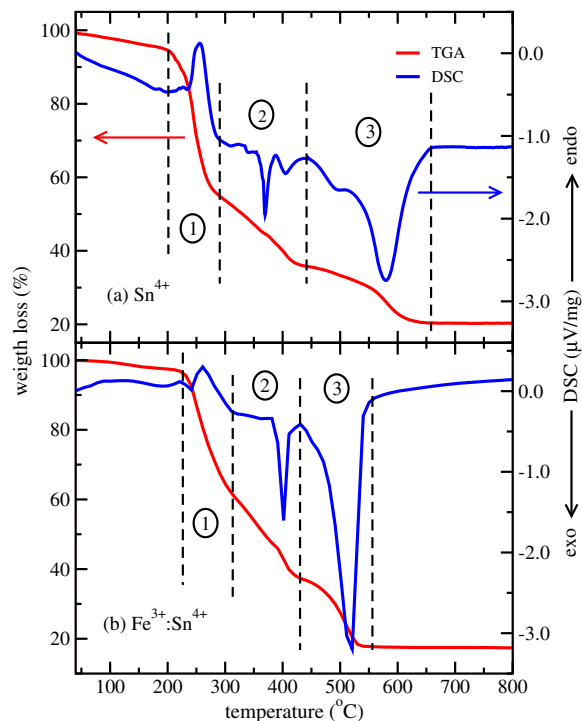

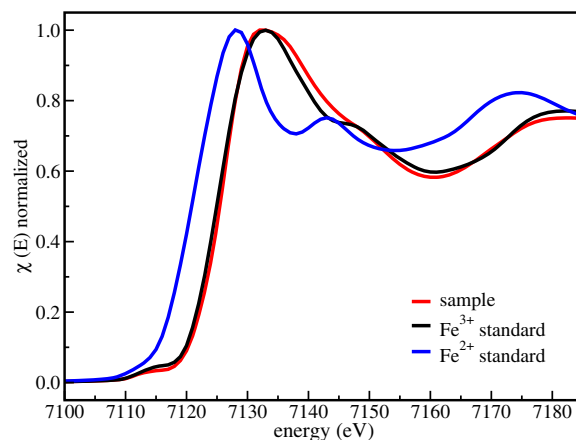**Fig. 2** TGA/DSC curves of **a** undoped and **b** Fe–doped SnO_2 precursor powders

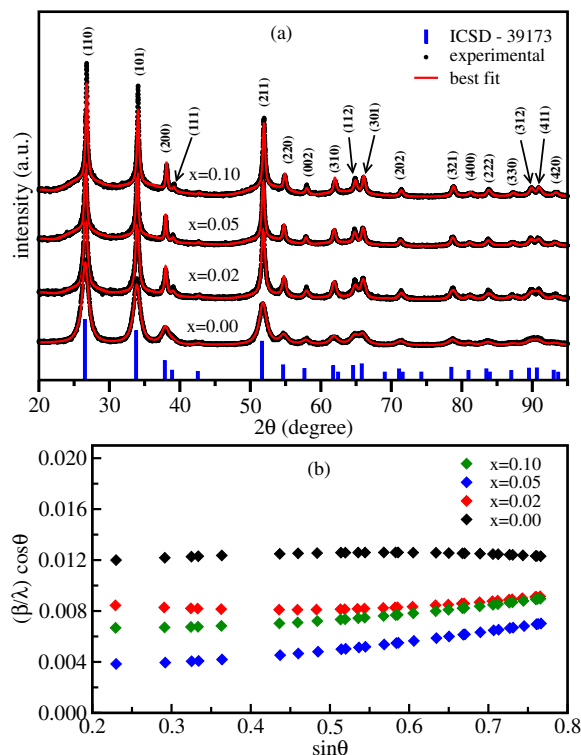**Fig. 3** Fe K-edge XANES spectra of a Fe–doped SnO_2 sample and reference compounds

Fig. 4 **a** X-ray diffraction patterns of $Sn_{1-x}Fe_xO_{2-y}$ nanoparticles. Dots and solid lines are the experimental data and best fits respectively. Bars represent the ICSD-39173 standard pattern. **b** Williamson-Hall curves

No impurity phase was found. The absence of secondary phase is attributed at efficiency of the proteic sol–gel method in yielding samples with dopants that are homogeneously distributed without clustering or segregation.

Lattice parameters, average crystallite size, and residual microstrain obtained from Rietveld refinement and Williamson-Hall correction are shown in Table 1. All samples showed crystallite size in the nanometer range with negligible levels of microstrain. The average cell volume of sample with $x = 0.02$ is larger than that of the undoped sample, despite the presence of oxygen vacancies and the smaller ionic radius of Fe^{3+} 0.64 Å) when compared to Sn^{4+} (0.69 Å). This increase can be explained by the stress created in the crystal lattice after the introduction of iron (Fang et al. 2008; Ferrari et al. 2016). Further increase in Fe content ($x = 0.05$ and 0.10), on the other hand, leads to a slight but consistent average cell volume decrease. For larger amounts of doping, oxygen vacancies and the smaller Fe^{3+} radius seem to overcompensate the lattice stress. These results suggest substitutional doping of SnO_2 with Fe^{3+}.

FT–IR spectroscopy

SnO_2 has the rutile structure crystallizing in the space group $P4_2/mnm$, which has a unit cell that consists of two tin and four oxygen atoms. The six unit cell atoms give a total of 18 branches for the vibration modes in the first Brillouin's zone. At the center of Brillouin zone, the symmetry of the modes is distributed according to the factor group D_{4h} as (Katyiyar et al. 1971; Diéguez et al. 2001):

$$\Gamma = A_{1g} + A_{2g} + A_{2u} + B_{1g} + B_{2g} + \\ 2\,B_{1u} + E_g + 3\,E_u. \quad (1)$$

X-ray diffration

Figure 4 shows (a) XRD patterns and (b) Williamson-Hall curves of $Sn_{1-x}Fe_xO_{2-y}$ ($x = 0$, 0.02, 0.05, and 0.10) samples. XRD patterns (black dots) were analyzed by the Rietveld refinement technique and the best fits are shown as solid red lines. All diffraction peaks correspond to the rutile-type tetragonal structure of SnO_2 of the ICSD-39173 standard pattern.

Table 1 Lattice parameters, average crystallite size, and residual microstrain of $Sn_{1-x}Fe_xO_{2-y}$ samples

x	$a = b$ (Å)	c (Å)	volume (Å³)	D_S (nm)	D_{WH} (nm)	ϵ (%)
0.00	4.740	3.185	71.55	8.0	8.0	0.01
0.02	4.746	3.189	71.83	12.0	13.0	0.07
0.05	4.743	3.187	71.70	19.0	54.0	0.25
0.10	4.742	3.183	71.60	13.0	19.0	0.17

D_S is the average crystallite size calculated by the Scherrer equation. D_{WH} and ϵ are average crystallite sizes and residual microstrain calculated by the Williamson-Hall method

The modes belonging to the A_{1g} and B_{1g} irreducible representations are Raman active, while those belonging to the A_{2u} and E_u irreducible representations are infrared active. FT–IR spectra of $Sn_{1-x}Fe_xO_{2-y}$ samples are shown in Fig. 5.

The spectrum of undoped SnO_2 shows the presence of two peaks: one of low intensity at ~470 cm^{-1}, and another of high intensity around 610 cm^{-1}. The absorption bands of Fe-doped SnO_2 are shifted to higher regions of the spectra in relation to those assigned to the undoped sample. The first peak is associated with the symmetric stretching of Sn–O and the second mode is associated with the anti-symmetric stretching of Sn–O. Although absorption peaks should also be expected at approximately 240 and 300 cm^{-1} in the infrared spectrum of undoped SnO_2, our experimental setup did not allow us their observation; as a consequence, our analysis is centered on the stretching vibrations of Sn–O.

The changes observed in the shape, width, and positions of FT–IR peaks are attributed to the variation in the local defects, grain size, and shape of the nanoparticles (Katyiyar et al. 1971; Diéguez et al. 2001). The absorption peaks observed from the doped samples revealed only the peak attributed to the pure SnO_2 phase. No absorption bands of secondary phases were detected. FT–IR analysis confirms the formation of single-phased $Sn_{1-x}Fe_xO_{2-y}$ nanoparticles, which is in good agreement with the XRD analysis.

Mössbauer spectroscopy

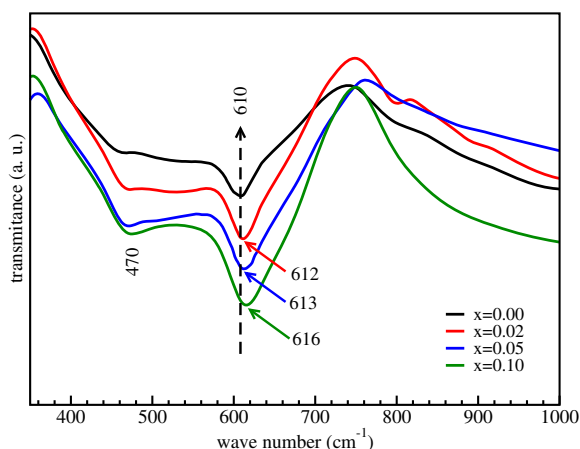Figure 6 shows Mössbauer spectra of $Sn_{1-x}Fe_xO_{2-y}$ samples and best fits with the respective hyperfine parameters listed in Table 2. Best fits were achieved with two paramagnetic doublets assigned to Fe^{3+} substituting for Sn^{4+} in distorted octahedral sites.

Isomer shift and quadrupole splitting values of both doublets increase with increasing Fe content, suggesting a higher structural and local disorder due to the Fe^{3+} incorporation into the crystalline structure of SnO_2. In addition, the larger values of quadrupole splitting found for doublet 2 are attributed to oxygen-deficient octahedral iron sites. In fact, oxygen-deficient octahedra carry enlarged electric field gradients and consequently larger values of quadrupole splitting (Beltran et al. 2010; Ferrari et al. 2016; Ribeiro et al. 2012). The large area of doublet 2 in the spectrum of nanoparticles with Fe content of 10 at% reveals a very high number of oxygen vacancies.

Mössbauer spectroscopy results confirm substitutional doping of Fe^{3+} in the SnO_2 host matrix as suggested by XRD results. They also indirectly confirm the presence of oxygen vacancies in doped samples.
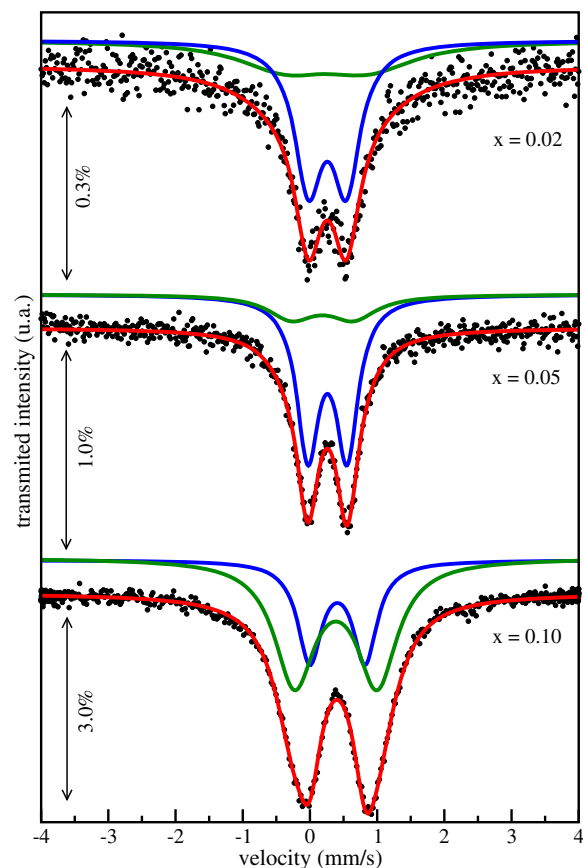

Fig. 6 Mössbauer spectra of $Sn_{1-x}Fe_xO_{2-y}$ samples with best fits to the data

Fig. 5 FT–IR spectra of $Sn_{1-x}Fe_xO_{2-y}$ samples

Table 2 Hyperfine parameters obtained from best fits to Mössbauer spectra of $Sn_{1-x}Fe_xO_{2-y}$ samples

x	Doublet 1				Doublet 2			
	δ mm/s	Δ mm/s	Γ mm/s	Area %	δ mm/s	Δ mm/s	Γ mm/s	Area %
0.02	0.36	0.56	1.66	61.0	0.36	1.25	1.66	39.0
0.05	0.37	0.58	0.40	76.0	0.29	0.92	0.40	24.0
0.10	0.52	0.82	0.43	32.5	0.49	1.23	0.73	67.5

δ, Δ, and Γ are isomer shift, quadrupole splitting, and line width, respectively. Uncertainties on δ, Δ, and Γ values are smaller than 0.02 mm/s and on area values are smaller than 0.5%
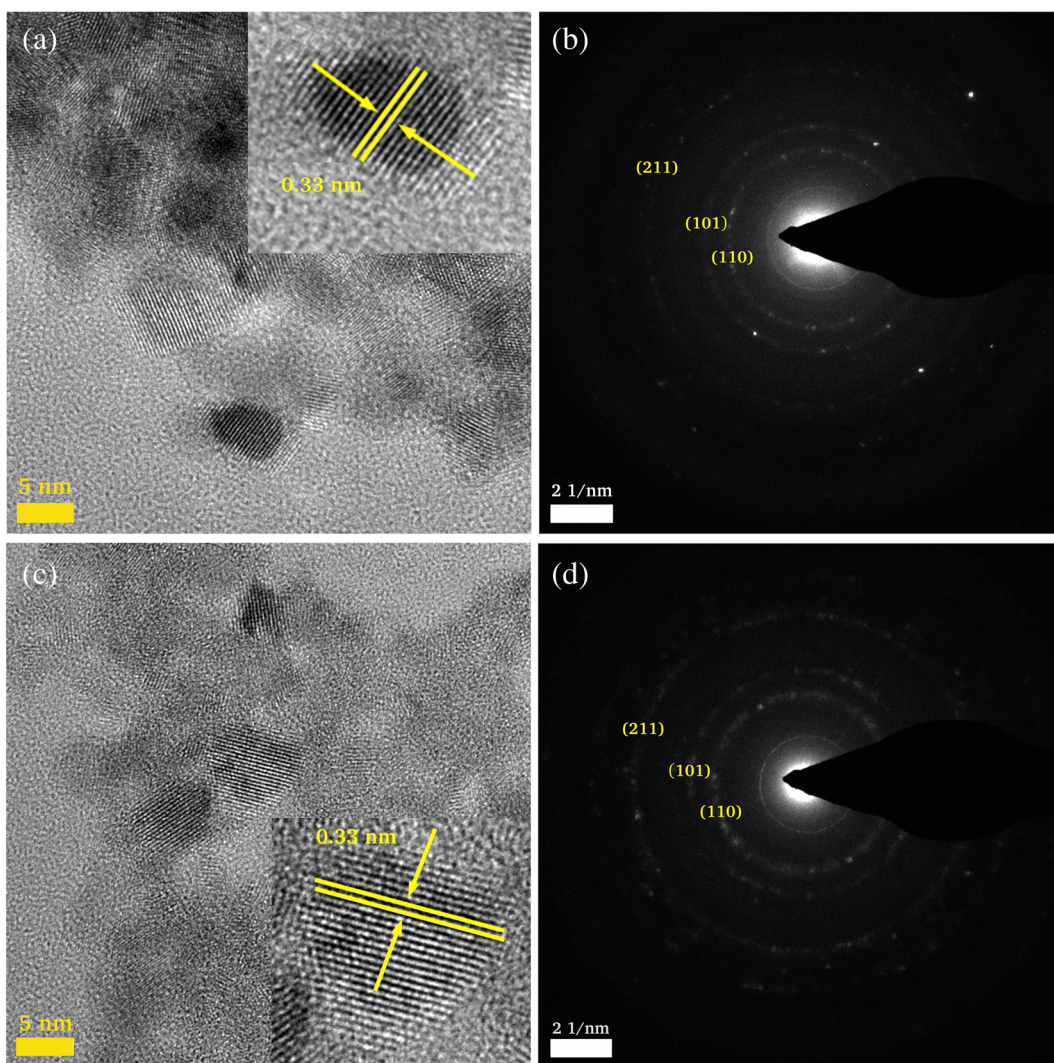

Fig. 7 TEM images and corresponding selected area electron diffraction (SAED) pattern of **a**, **b** undoped and **c**, **d** Fe–doped SnO_2 samples. Inset: Zoomed-in images

Transmission electron microscopy

Figure 7 shows TEM images and their corresponding selected area electron diffraction (SAED) patterns of (a, b) undoped and (c, d) Fe-doped SnO_2 (10 at% of Fe) samples. From the TEM images, it can be seen that nanoparticles have an approximate spherical morphology with an average diameter of about 10 nm, in agreement with the sizes obtained from the XRD data. High magnification of the nanoparticles are shown on the inset of Fig. 7a, c. The interplanar distance was estimated as approximately 0.33 ± 0.02 nm, which corresponds to the {110} diffraction planes of the rutile-type structure. It is worth mentioning that these diffraction planes are commonly found in nano-sized SnO_2 systems. These values are in agreement with those reported in the literature (Pal et al. 2015; Aragón et al. 2016).

UV–Vis spectroscopy

UV–Vis spectroscopy is an excellent diagnostic tool for optical characterization of powdered, crystalline, and nanostructure materials in different spectral ranges. In particular, measuring the absorption coefficient for various energies gives information about the band gaps of the material (Alibe et al. 2016, 2017, 2018; Saleh et al. 2016; Chetri and Choudhury 2013; Lopez and Gomez 2012). Knowledge of these band gaps is extremely important for understanding the electrical properties of a semiconductor, and is therefore of great practical interest.

The energy gap can be obtained from UV–Vis measurements by applying the Kubelka-Munk (KM) method (Kubelka and Munk 1931). The KM theory is generally used for analyzing the diffuse reflectance spectra obtained from weakly absorbing samples and is based on the following equation (Alibe et al. 2017; Saleh et al. 2016; Chetri and Choudhury 2013):

$$F(R) = \frac{(1-R)^2}{2R}, \qquad (2)$$

where R is the reflectance. The absorbance $F(R)$ is proportional to the absorption coefficient α, given by (Alibe et al. 2016, 2018; Saleh et al. 2016; López and Gómez 2012):

$$\alpha = \frac{A(h\nu - E_g)^n}{h\nu}, \qquad (3)$$

where A is an absorption constant, $h\nu$ is the incident photon energy, and E_g is the optical energy band gap. The value of n depends on the type of transition. It is equal to 1/2 for direct allowed transitions, 2 for indirect allowed transitions, 3/2 for direct forbidden transitions, and 3 for indirect forbidden transitions (Davis and Mott 1970). Combining Eqs. 2 and 3, we obtain:

$$[F(R)\,h\nu]^2 \propto h\nu - E_g. \qquad (4)$$

Band gap energies are obtained by extrapolating the linear part of the $[F(R)\,h\nu]^2 \times h\nu$ plot to the photon energy axis. This is known as the Tauc method (Tauc et al. 1966).

Figure 8a shows absorbance spectra of $Sn_{1-x}Fe_xO_{2-y}$ samples. The curves display an absorption band in the ultraviolet region near the visible light range. It can be seen that the spectra tend to shift to higher wavelength with the increase of the dopant concentration. This could be attributed to the charge-transfer transitions between the Fe^{3+} d-electrons and the SnO_2 conduction or valence band (Fang et al. 2008).
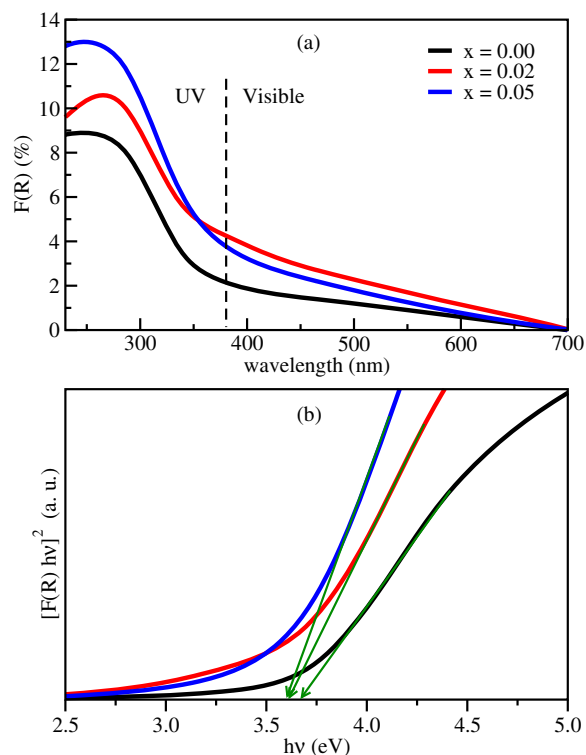
Fig. 8 **a** UV–Vis absorbance spectra of $Sn_{1-x}Fe_xO_{2-y}$ samples and **b** $[F(R)\,h\nu]^2 \times h\nu$ Tauc plots

Tauc plots are shown in Fig. 8b. The band gap energy values found were about 3.7 eV for the pristine SnO_2 samples and 3.6 eV for the $Sn_{1-x}Fe_xO_{2-y}$ samples with $x = 0.02$ and 0.05. It was observed that for these concentrations of dopant the band gap remains virtually unchanged. These optical band gap values are in agreement with those reported by other researcher groups (Saleh et al. 2016; Chetri and Choudhury 2013; Fang et al. 2008).

Conclusions

The proteic sol–gel method was successfully applied to produce nanoparticles of $Sn_{1-x}Fe_xO_{2-y}$ ($x = 0.00$, 0.02, 0.05, and 0.10). XANES analyses confirmed 3+ as the oxidation state of doping Fe ions. XRD results showed the presence of a single rutile SnO_2 nanostructured phase which was confirmed by FT–IR analyses. Variations in average unit cell volume with dopant concentration suggested substitutional doping of SnO_2 with Fe^{3+}. This claim was confirmed by Mössbauer spectroscopy as all spectra were comprised of doublets consistent with Fe^{3+} in octahedral coordination occupying Sn^{4+} crystallographic sites. Mössbauer results indirectly confirmed the existence of oxygen vacancies. TEM results showed nanoparticles with spherical shape and average diameter between 5 and 10 nm. UV–Vis spectroscopy showed that band gaps of SnO_2 were not affected by the presence of Fe.

The experimental results presented in this paper are useful for the advancement and understanding of structural, morphological, and optical properties of O-DMS materials based on Fe-doped SnO_2 nanoparticles. These compounds also represent a promising path to applications on technologies such as photovoltaic solar cells.

Compliance with Ethical Standards We declare that we agree with the ethical standards of the journal.

Conflict of interest The authors declare that they have no conflict of interest.

References

Ahmed SA (2010) Room-temperature ferromagnetism in pure and Mn doped SnO_2. Solid State Commun 150:2190–2193. https://doi.org/10.1016/j.ssc.2010.08.029

Alibe IM, Matori KA, Saion E, Alibe AM, A M ZaidMHM, Ghapur Engku EAA (2016) A facile synthesis of amorphous silica nanoparticles by simple thermal treatment route. Dig J Nanomater Biostruct 11:1155–1164. http://psasir.upm.edu.my/id/eprint/54842

Alibe IM, Matori KA, Saion E, Ali AM, Zaid MHM (2017) The Influence of calcination temperature on structural and optical properties of ZnO nanoparticles via simple polymer synthesis route. Sci Sinter 49:263–275. https://doi.org/10.2298/SOS1703263A

Alibe IM, Matori KA, Sidek HAA, Yaakob Y, Rashid U, Alibe AM, Zaid MHM, Khiri MZA (2018) Effects of calcination holding time on properties of wide band gap willemite semiconductor nanoparticles by the polymer thermal treatment method. Molecules 23:873. https://doi.org/10.3390/molecules23040873

Aragón FH, Coaquira JAH, Nagamine LCCM, Cohen R, da Silva SW, Morais PC (2016) Thermal-annealing effects on the structural and magnetic properties of 10% Fe-doped SnO_2 nanoparticles synthetized by a polymer precursor method. J Mag Magn Mater 375:74–79. https://doi.org/10.1016/j.jmmm.2014.09.052

Beltrán JJ, Sánchez LC, Osorio J, Tirado L, Baggio-Saitovich EM, Barrero CA (2010) Crystallographic and magnetic properties of Fe-doped SnO_2 nanopowders obtained by a sol-gel method. J Mater Sci 45:5002–5011. https://doi.org/10.1007/s10853-010-4454-z

Chang C-H, Gong M, Dey S, Liu F, Castro RHR (2015) Thermodynamic Stability of SnO_2 Nanoparticles: The Role of Interface Energies and Dopants. J Phys Chem C 119:6389–6397. https://doi.org/10.1021/jp512969k

Chetri P, Choudhury A (2013) Investigation of optical properties of SnO_2 nanoparticles. Phys E 47:257–263. https://doi.org/10.1016/j.physe.2012.11.011

Davis EA, Mott NF (1970) Conduction in non-crystalline systems V. Conductivity and optical absorption and photoconductivity in amorphous semiconductors. Philos Mag A 22:903922. https://doi.org/10.1080/14786437008221061

Diéguez A, Romano-Rodríguez A, Vilà A, Morante JR (2001) The complete Raman spectrum of nanometric SnO_2 particles. J Appl Phys 90:1550. https://doi.org/10.1063/1.1385573

Fang LM, Zu XT, Li ZJ, Zhu JS, Liu CM, Zhou WL, Wang LM (2008) Synthesis and characteristics of Fe^{3+}-doped SnO_2 nanoparticles via sol-gel-calcination or sol-gel-hydrothermal route. J Alloys Compd. 454:261–267. https://doi.org/10.1016/j.jallcom.2006.12.014

Feng Y, Ji W-X, Huang B-J, Chen X-L, Li F, Li P, Zhang C-W, Wang P-J (2015) The magnetic and optical properties of 3d transition metal doped SnO_2 nanosheets. RSC Adv 5:24306–24312. https://doi.org/10.1039/C5RA00788G

Ferrari S, Pampillo LG, Saccone FD (2016) Magnetic properties and environment sites in Fe doped SnO_2 nanoparticles. Mater Chem Phys 177:206–212. https://doi.org/10.1016/j.matchemphys.2016.04.020

Inpasalin MS, Choubey RK, Mukherjee S (2016) Evidence of Bound Magnetic Polaron-Mediated Weak Ferromagnetism in co-doped SnO_2 Nanocrystals: Microstructural, Optical, Hyperfine, and Magnetic Investigations. J Elect Mater 45:3562–3569. https://doi.org/10.1007/s11664-016-4520-7

Katyiyar RS, Dawson P, Hargreave MM, Wilkinson GR (1971) Dynamics of the rutile structure III. Lattice dynamics, infrared and Raman spectra of SnO_2. J Phys C: Solid St Phys 4:2421. http://stacks.iop.org/0022-3719/4/i=15/a=027

Kubelka P, Munk F (1931) Ein beitrag zur optik der farbanstriche. Z Tech Phys 12:593–601

Liu J, Li X, Chen X, Niu H, Han X, Zhang T, Lin H, Qu F (2016) Synthesis of SnO_2/In_2O_3 hetero-nanotubes by coaxial-electrospinning method for enhanced formaldehyde response. New J Chem 40:1756–1764. https://doi.org/10.1039/C5NJ02337H

Liu X, Lu Q, Zhu C, Liu S (2015) Liu, Enhanced photocatalytic activity of α-Fe_2O_3/Bi_2WO_6 heterostructured nanofibers prepared by electrospinning technique. RSC Adv 5:4077–4082. https://doi.org/10.1039/C4RA11613E

López R, Gómez R (2012) Band–gap energy estimation from diffuse reflectance measurements on sol–gel and commercial TiO_2: a comparative study. J Sol–Gel Sci Technol 61:1–7. https://doi.org/10.1007/s10971-011-2582-9

Mehraj S, Ansari MS, Alimuddin (2013) Rutile-type Co doped SnO_2, diluted magnetic semiconductor nanoparticles: Structural, dielectric and ferromagnetic behavior. Physica B 430:106–113. https://doi.org/10.1016/j.physb.2013.08.024

Mehraj S, Ansari MS, Alimuddin (2015) Structural, electrical and magnetic properties of (Fe, Co) co-doped SnO_2, diluted magnetic semiconductor nanostructures. Physica E 65:84–92. https://doi.org/10.1016/j.physe.2014.08.016

Meneses CT, Flores WH, Garcia F, Sasaki JM (2007) A simple route to the synthesis of high-quality NiO nanoparticles. J Nanopart Res 9:501–505. https://doi.org/10.1007/s11051-006-9109-2

Mueller F, Bresser D, Chakravadhanula VSK, Passerini S (2015) Fe-doped SnO_2 nanoparticles as new high capacity anode material for secondary lithium-ion batteries. J Power Sources 299:398–402. https://doi.org/10.1016/j.jpowsour.2015.08.018

Oganisian K, Hreniak A, Sikora A, Gaworska-Koniarek D, Iwan A (2015) Synthesis of iron doped titanium dioxide by sol-gel method for magnetic applications. Proc Appl Ceram 9:43–51. https://doi.org/10.2298/PAC1501043O

Ohno H (2010) A window on the future of spintronics. Nat Mater 9:952–954. https://doi.org/10.1038/nmat2913

Othmen WB, Sdiri N, Elhouichet H, Férid M (2016) Study of charge transport in Fe-doped SnO_2 nanoparticles prepared by hydrothermal method. Mater Sci Semicon Proc 52:46–54. https://doi.org/10.1016/j.mssp.2016.05.010

Pal M, Bera S, Jana S (2015) Sol-gel based simonkolleite nanopetals with SnO_2 nanoparticles in graphite-like amorphous carbon as an efficient and reusable photocatalyst. RSC Adv 5:75062–75074. https://doi.org/10.1039/C5RA12322D

Pereira MS, Lima FAS, Ribeiro TS, da Silva MR, Almeida RQ, Barros EB, Vasconcelos IF (2017a) Application of Fe-doped SnO_2 nanoparticles in organic solar cells with enhanced stability. Opt Mater 64:548–556. https://doi.org/10.1016/j.optmat.2017.01.023

Pereira MS, Lima FAS, Silva CB, Freire PTC, Vasconcelos IF (2017b) Structural, morphological and optical properties of SnO_2 nanoparticles obtained by a proteic sol-gel method and their application in dye-sensitized solar cells. J Sol-Gel Sci Technol 84:206–213. https://doi.org/10.1007/s10971-017-4488-7

Ribeiro TS, Sasaki JM, Vasconcelos IF (2012) Structural disorder of ball-milled, nanosized, Fe-doped SnO_2: X-ray diffraction and Mössbauer spectroscopy characterization. J Mater Sci 47:2630–2636. https://doi.org/10.1007/s10853-011-6088-1

Rietveld HM (1967) Line Profiles of neutron powder-diffraction peaks for structure refinement. Acta Cryst 22:151–152. https://doi.org/10.1107/S0365110X67000234

Rietveld HM (1969) A profile refinement method for nuclear and magnetic structures. J Appl Cryst 2:65–71. https://doi.org/10.1107/S0021889869006558

Saleh SA, Ibrahim AA, Mohamed SH (2016) Structural and optical properties of nanostructured Fe-doped SnO_2. Acta Physica Polonica A 129:1220–1225. https://doi.org/10.12693/APhysPolA.129.1220

Shayesteh SF, NosratiThe R (2015) Structural and magnetic properties of diluted magnetic semiconductor $Zn_{1-x}Ni_xO$ nanoparticles. J Supercond Nov Magn 28:1821–1826. https://doi.org/10.1007/s10948-015-2950-8

Song H-J, Jia XH, Li N, Yang X-F, Tang H (2012) Synthesis of α-Fe_2O_3 nanorod/graphene oxide composites and their tribological properties. J Mater Chem 22:895–902. https://doi.org/10.1039/C1JM13740A

Sun J, Sun P, Zhang D, Xu J, Liang X, Liu F, Lu G (2014) Growth of SnO_2 nanowire arrays by ultrasonic spray pyrolysis and their gas sensing performance. RSC Adv 4:43429–43435. https://doi.org/10.1039/C4RA05682E

Tauc J, Grigorovici R, Vancu A (1966) Optical properties and electronic structure of amorphous germanium. Phys Status Solidi B 15:627–637. https://doi.org/10.1002/pssb.19660150224

Toby BH (2001) EXPGUI, a graphical user interface for GSAS. J Appl Cryst 34:210–213. https://doi.org/10.1107/S0021889801002242

Tran V-H, Khan R, Lee I-H, Lee S-H (2018) Low-temperature solution-processed ionic liquid modified SnO_2 as an excellent electron transport layer for inverted organic solar cells. Sol Energy Mater Sol Cells 179:260–269. https://doi.org/10.1016/j.solmat.2017.12.013

Williamson GK, Hall WH (1953) X-ray line broadening from filed aluminium and wolfram. Acta Metall 1:22–31. https://doi.org/10.1016/0001-6160(53)90006-6

Zhao B, Fan B, Xu Y, Shao G, Wang X, Zhao W, Zhang R (2015) Preparation of honeycomb SnO_2 foams and configuration-dependent microwave absorption features. ACS Appl Mater Interfaces 7:26217–26225. https://doi.org/10.1021/acsami.5b08383